STRENGTH
AND PLASTICITY

Effect of Rotation Speed on Performance of Friction Stir Welded Spray-Formed 7055 Aluminum Alloy

Yumo Jiang[a], Yong Zhao[a], *, Zhixia Zhao[a], Shengchong Ma[a], and Keng Yan[a]

[a] Country Provincial key Lab of Advanced Welding Technology, Jiangsu University of Science and Technology, Zhenjiang Jiangsu, 212003 China
*e-mail: yongzhao418@just.edu.cn

Abstract—Ultra-high-strength spray-formed 7055 aluminum alloy was welded at different rotation speeds with a constant welding speed of 175 mm/min by friction stir welding, the aim of which was to assess the effects of rotation speed on the microstructure, properties, and phase evolution of the joint. In addition, the effects of strengthening phase distribution on the joint properties were also evaluated.

INTRODUCTION

Spray-formed ultra-high-strength aluminum alloys have been widely used in the aerospace and automotive industries due to their excellent properties [1—4]. These alloys have a high solution of Zn and the microstructural G.P. zones, as well as the η' metastable and η equilibrium phases enhance the mechanical properties of the alloys. The performance of FSW-ed joint is determined by the heat input during the welding process influenced by experimental parameters, such as the welding speed and rotational speed [5—9]. Wang et al. illustrated the adjustment strategy for the spray-formed 7055 aluminum alloy that underwent friction stir welding by changing the rotation or traveling speeds. These parameters significantly made one possible to guide underwater friction stir welding, analyze the mechanism of strengthening in the body of the underwater friction stir welded joint and showed that it could retain the original strengthening phase in base materials [10—14]. Although the underwater welding method can control the heat input, it has some limitations in engineering application. In this study, an ultra-high-strength spray-formed 7055 aluminum alloy was welded at different rotation speeds with a constant welding speed of 175 mm/min to assess the effects of rotation speed on the microstructure, properties, and phase evolution of the joint. In addition, the effects of strengthening phase distribution on the joint properties were also evaluated.

EXPERIMENTAL

Table 1 shows the chemical composition of base metal (BM). The plate was cut into 150 × 100 × 4 mm pieces, and then a butt joint was formed. The plates were friction stir welded by a FSW-3LM-002 instrument. The welding direction was perpendicular to the extrusion direction of the workpiece. The welding speed was maintained constant at 175 mm/min, and the rotation speeds were 700, 900, 1100, 1300, and 1500 rpm. The pin tool was composed of a shoulder with a diameter of 12 mm and a length of 3.9 mm, and the pin was 3 mm in diameter. A constant angle of tilt was maintained at 2.5° during the welding process. After grinding and polishing, Keller's reagent (2, 3, 5, and 190 mL of HF, HCl, HNO_3, and deionized water) was used to etch metallographic samples for approximately 30 s. The weld cross-sections of the specimens under different parameters were observed and measured using an MSDVHX1000 ultra-deep field three-dimensional (3D) microscope. Different areas of the joint were observed under a metallographic microscope. The measurement module of the software, Image-Pro Plus 6.0, was introduced in this study to measure the grain size by its micrograph. JSM-6460 scanning electron microscope and energy dispersive spectrometer (SEM&EDS) was utilized to assess the morphology of the fracture and image weld areas at high magnification, and detect the elemental contents of the samples. Precipitation in the joints was assessed by differential scanning calorimetry (DSC; heating rate, 40°C/min; temperature range, 100—520°C) and

Table 1. Chemical composition of base metal (wt %)

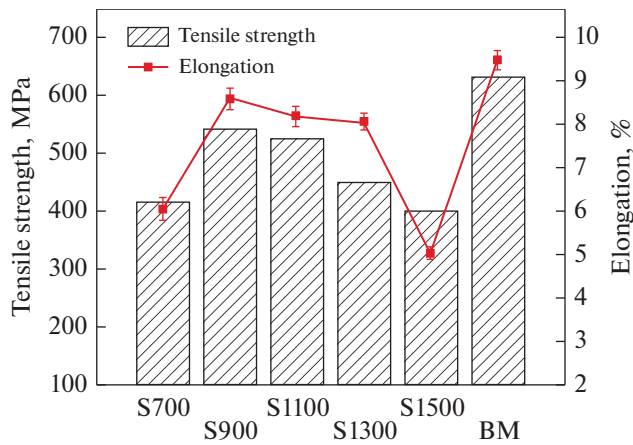| Zn	Mg	Cu	Si	Fe	Al
7.6—8.6	1.8—2.2	2.0—2.5	0.10	0.15	Bal.

Fig. 1. Tensile test results at different rotation speed.

X-ray diffraction (XRD; scan angle range, $20°-110°$; scanning speed, $4°/\text{min}$). The abbreviation NZ and HAZ represent the nugget zone and heat-affected zone, respectively. In this study, S1 represents S700F175, which means the rotation speed is 700 rpm and the welding speed is 175 mm/min; S2 represents S900F175, which means the rotation speed is 900 rpm and the welding speed is 175 mm/min; S3 represents S1100F175, which means the rotation speed is 1100 rpm and the welding speed is 175 mm/min; S4 represents S1300F175, which means the rotation speed is 1300 rpm and the welding speed is 175 mm/min; S5 represents S1500F175, which means the rotation speed is 700 rpm and the welding speed is 175 mm/min.

RESULTS

Figure 1 shows the tensile test results at different rotation speeds. At a constant traveling speed of F175, the tensile strength and elongation increased first and then decreased with the rotation speed from 700 to 1500 rpm. At 900 rpm, values of both parameters peaked; maximum tensile strength and elongation of all joints were 542 MPa and 9%, up to 85 and 90% of the BM. At 1500 rpm, the tensile strength and elongation were 400 MPa and 5%, up to 63 and 52% of the BM. The low rotation speed could not generate sufficient heat input to make the complete joint, effectuating poor properties. High rotation speed caused overheating, which made the recrystallized grains be coarsened and then lead to the poor properties.

Figure 2 shows the fracture positions and profiles of the tensile specimens. Two characteristic fractures of the joint were noted. At the rotation speeds of 700 and 900 rpm, respectively, the cross-section was flat at $45°$ with the fracture positioned in the HAZ. The fracture located on the edge of the NZ at the rotation speeds of 1100 and 1300 rpm, respectively. The fracture located in the NZ at the rotation speed of 1500 rpm. Multiple small dimples in the second-phase particles can be found at 700 rpm in the fracture diagram. Some shallow pits were found in high magnification images, showing the intersection of the slip system while less open slip systems caused poor plasticity. At 900 rpm, large tearing edges existed between the tiny dimples that can be seen in the image. At 1100 rpm, the cross-section was slipped into two layers. A tearing edge can been found in the upper layer, while the lower layer is granular. In the high magnification image, the morphology of the two parts was similar, and the particles in the upper layer were large. At 1300 rpm, the cross-section was also split into two layers, and the morphology of the two layers was similar. The specimen exhibited the transgranular fracture. At 1500 rpm, the fracture occurred in the NZ and the morphology is similar to that at 1300 rpm with a large particle outline.

The figure shows that the grains in the NZ of S-2 (S900F175) were significantly smaller than those of S-5 (S1500F175), and the grains in the HAZ of S-2 were also smaller than those of S-5. During the process of friction stir welding, the material under the shoulder of the stirring head reached the dissolution temperature of the precipitation phase as a response to friction heat. However, this temperature was lower than the melting temperature of aluminum alloy that would effectuate the recrystallization of grains and redistribution of precipitation phase in friction stir. Compared to the HAZ of S-2, the precipitated phase in the NZ was relatively small, and the precipitation position was close to the grain boundary. However, the precipitation in the HAZ was large and precipitated mainly along the grain boundary. The Cu element precipitated more at the grain boundary than in the grain. In the HAZ of S-2, the Cu element precipitated more at the grain boundary, and the proportion of Cu that precipitated in the HAZ was much higher than that in the core area. However, many phases precipitated in the NZ of S-5, most of which were located along grain boundary, while only a few phases precipitated in the HAZ. The phases precipitated along the grain boundary would reduce the joint performance, especially the tensile performance. According to the analysis of the tensile properties of S-2 and S-5, as well as the fracture location and macroscopic morphology of the joint, it can be concluded that the fracture of S-2 was transgranular. The SEM figure shows that the phases precipitated along the grain boundary were not continuous, which altered the fracture path of the joint during the fracture process, and thus, the tearing edge appears in the fracture. However, S-5 shows an intergranular fracture. The SEM images showed many large pieces of precipitated phase along the boundary in the NZ of S-5, which reduced the tensile property of the joint. In addition, TEM was used to distinguish the phases (Fig. 4).
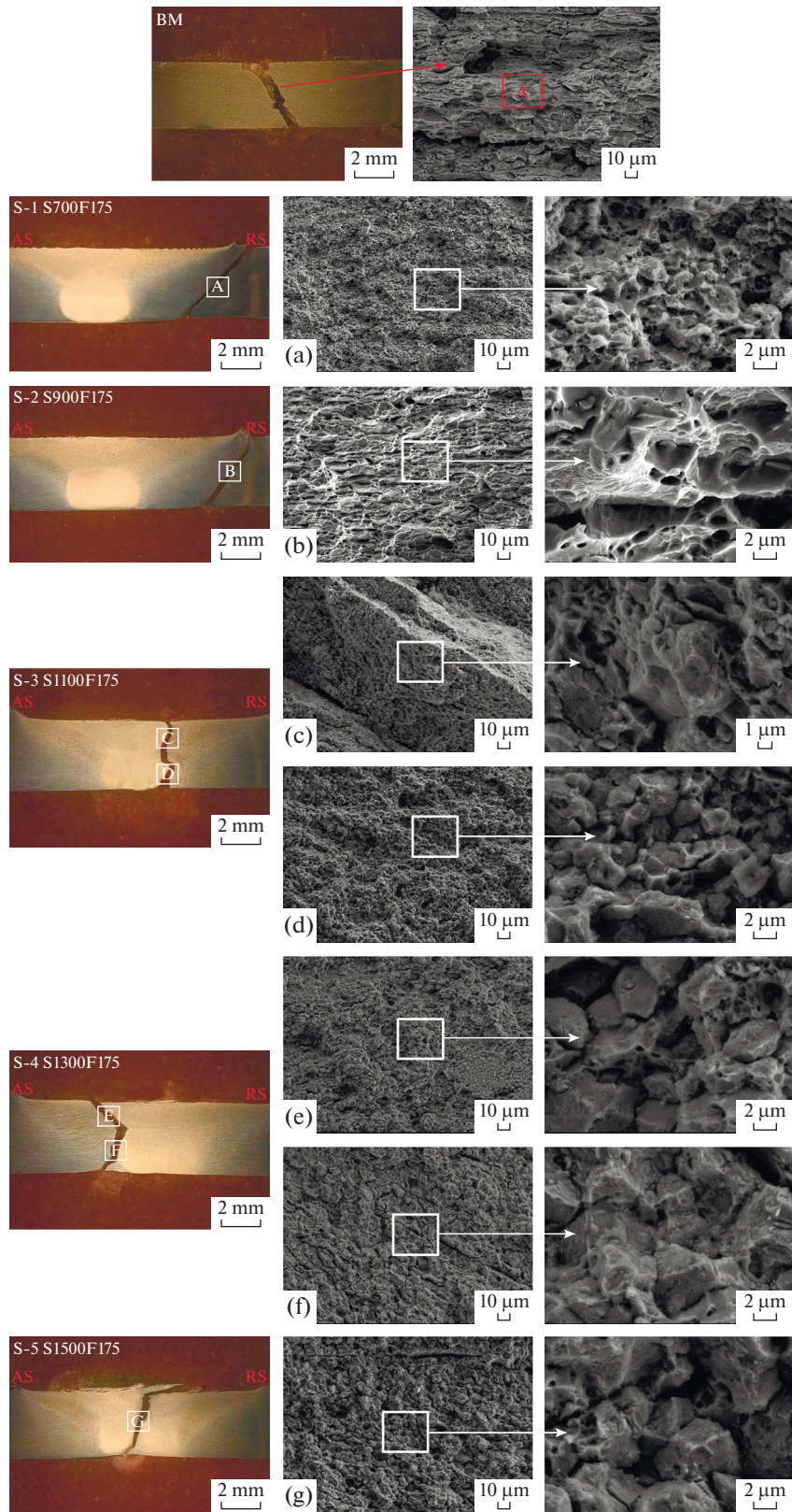
Fig. 2. Fracture position and morphology of the joints.

(a) Nugget zone of the sample S-5

NZ(S-2)

	Position 1			Position 2	
Element	Weight, %	Atom, %	Element	Weight, %	Atom, %
Al	75.72	87.03	Al	92.44	94.48
Zn	9.64	4.57	Zn	3.19	1.34
Mg	1.59	2.03	Mg	2.03	2.30
Cu	13.05	6.37	Cu	2.34	1.89
Total	100.00	100.00	Total	100.00	100.00

(b) Heat affected zone of S-5

HAZ-RS(S-2)

	Position 3			Position 4	
Element	Weight, %	Atom, %	Element	Weight, %	Atom, %
Al	41.85	62.13	Al	87.64	91.88
Zn	6.85	4.20	Zn	8.56	3.71
Mg	1.31	2.15	Mg	3.79	4.41
Cu	49.99	31.52	Cu	0	0
Total	100.00	100.00	Total	100.00	100.00

(c) Nugget zone of S-5

NZ(S-5)

	Position 1			Position 2	
Element	Weight, %	Atom, %	Element	Weight, %	Atom, %
Al	38.26	57.51	Al	71.88	83.83
Zn	9.90	6.14	Zn	8.68	4.18
Mg	3.17	5.29	Mg	2.97	3.84
Cu	48.67	31.07	Cu	16.47	8.16
Total	100.00	100.00	Total	100.00	100.00

(d) Heat affected zone of S-5

HAZ-RS(S-5)

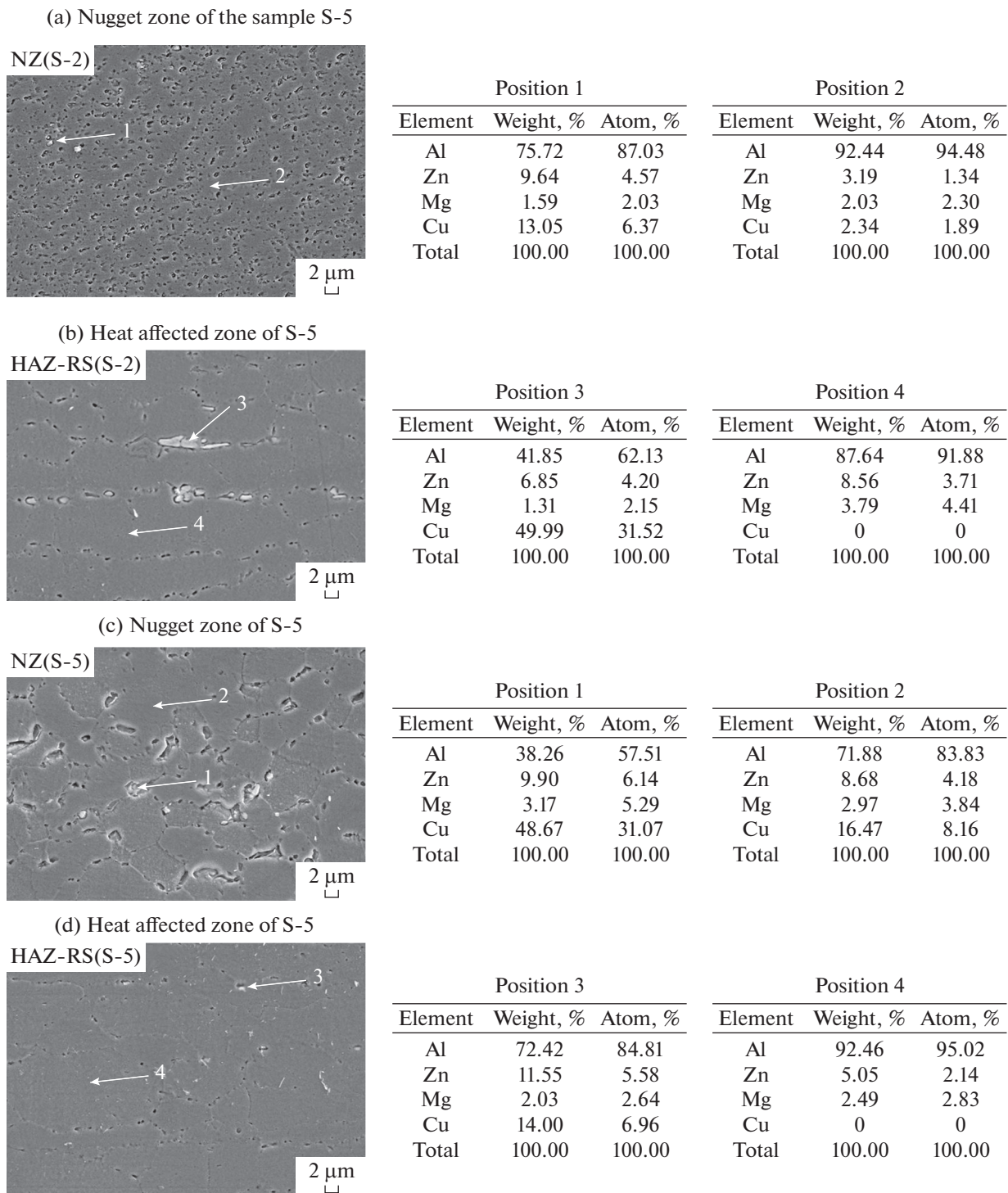|	Position 3			Position 4	
Element	Weight, %	Atom, %	Element	Weight, %	Atom, %
Al	72.42	84.81	Al	92.46	95.02
Zn	11.55	5.58	Zn	5.05	2.14
Mg	2.03	2.64	Mg	2.49	2.83
Cu	14.00	6.96	Cu	0	0
Total	100.00	100.00	Total	100.00	100.00

Fig. 3. Analysis results of SEM&EDS at the position of failure.

Figure 5 shows the XRD of HAZ and BM. The main strengthening phases were $MgZn_2$, Al_2Cu, and AlCuMg. Several phases precipitated in HAZ with the increase in the rotation speed for Al_2Cu, Al_2CuMg, and even the complex $Mg_{32}(Al,Zn)_{49}$. However, no complex phases precipitated in the NZ. Similar to the condition in HAZ, more phases precipitated in the NZ with the increase in the rotation speed.

Figure 6 shows the DSC curves of BM and joints at HAZ. The curve of the BM was concave under 250°C, suggesting a slow exothermic state, which indicated the precipitation of the solid solution phase in the BM.
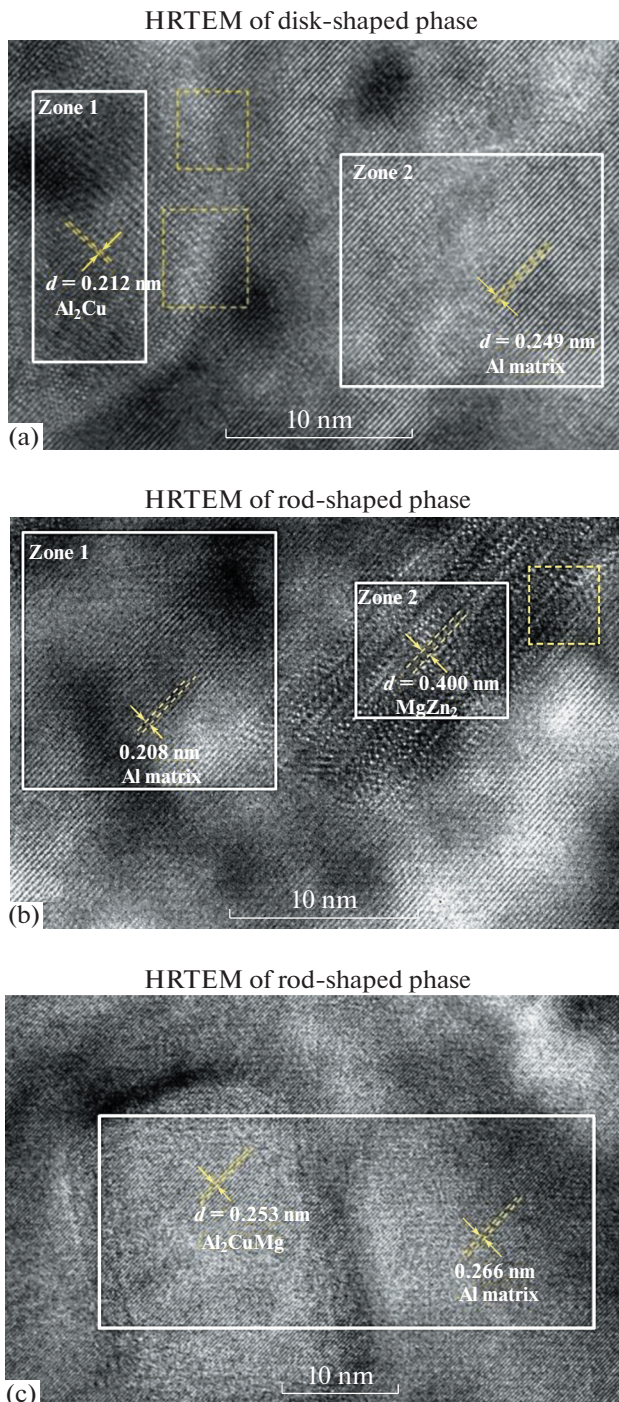
HRTEM of disk-shaped phase

HRTEM of rod-shaped phase

HRTEM of rod-shaped phase

Fig. 4. TEM analysis. (a) HRTEM of disk-shaped phase; (b) HRTEM of rod-shaped phase; (c) HRTEM of capsule-shaped phase.
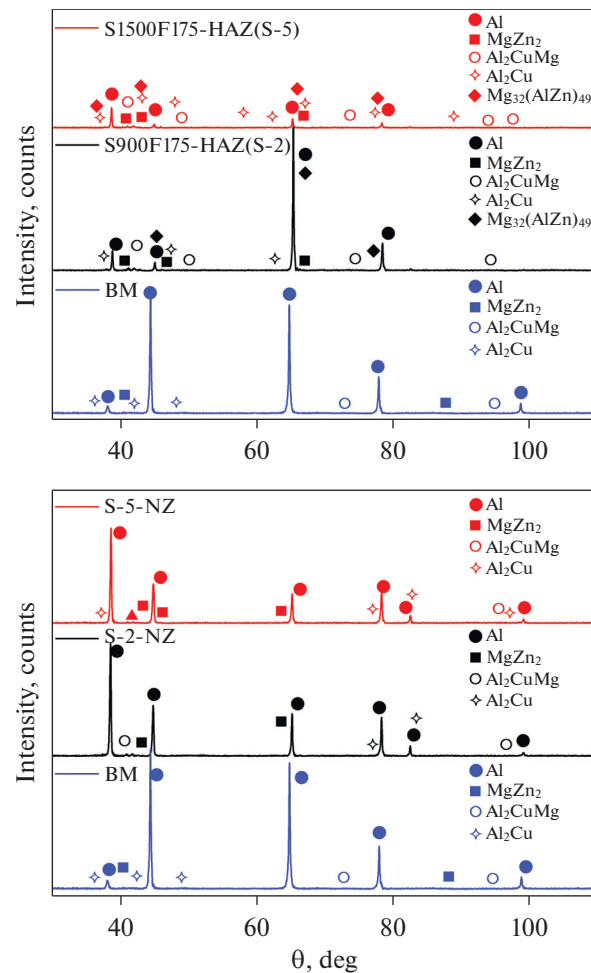

Fig. 5. XRD of the HAZ and the BM.

aroused by the structural transformation of Mg–Al phase. The two obvious endothermic peaks of S-5 represented the precipitation of Al–Cu phase during the transformation from GP zones (θ'') to θ' in HAZ. The peak at 487.47°C in HAZ indicated the dissolution of η'. "a" represents HAZ of S2 sample. "b" represents HAZ of S5 sample. "c" represents BM.

Figure 7 shows the DSC curves of BM and joints at the NZ. The peak near 238 and 275°C was aroused by the structural transformation of Mg–Al phase. Large quantities of Al–Cu phases were precipitated in HAZ at the rotation speed of 900 rpm, while those in NZ precipitated at the rotation speed of 1500 rpm. The precipitated phases were caused by overheating in the joint, which leads to the tensile failure. "a" represents HAZ of S2 sample. "b" represents HAZ of S5 sample. "c" represents BM.

Hardness profiles of the joints are shown in Fig. 8. The distribution and variation of hardness corresponded to the various regions of the joint. The minimum hardness values appeared in the HAZ, and the hardness value of the upper part of the NZ was high.
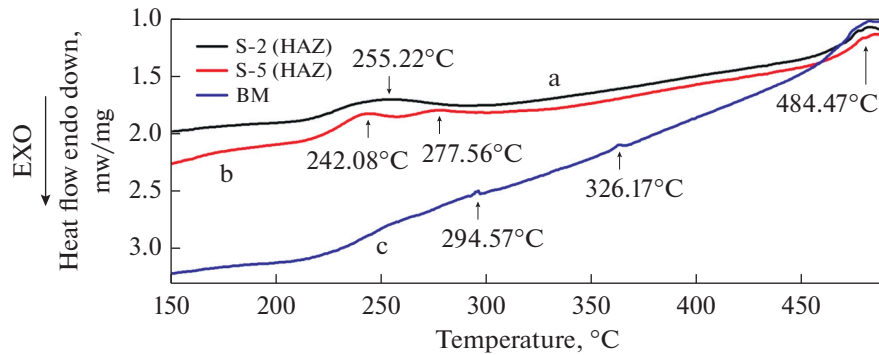
The DSC curve of the BM shows three tiny endothermic peaks, which represent the peaks of GP zones (294.57°C), θ (362.67°C), and η (478.01°C). S-2 had two obvious endothermic peaks at 255.22 and 487.47°C, respectively. The peak at 255.22°C was

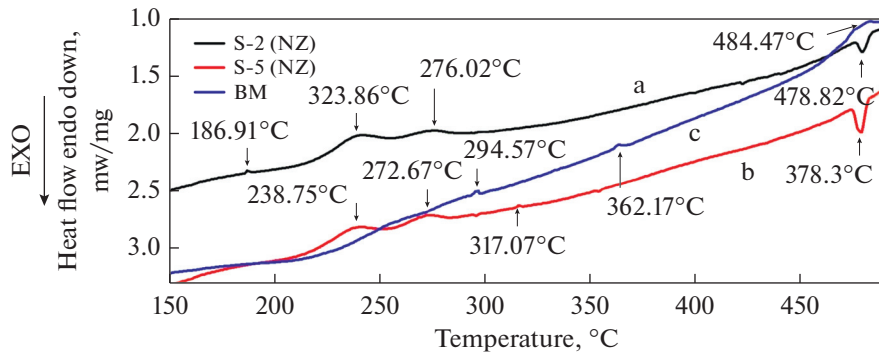**Fig. 6.** DSC curves of BM and joints at the heat affected zone.

Fig. 7. DSC curves of base metal and joints at NZ.

With the increase in the rotating speed of the stirring head, the HAZ of the joint gradually became larger, and the low-hardness area of the HAZ increased and then decreased. The fracture was located in the softening zone or the area where the hardness was uneven.

CONCLUSIONS

(1) The stirring affected area of the pin increased with increasing rotation speed. The NZ was characterized by fine equiaxed grains. With the increase in the welding speed from 700 rpm to 1500 rpm, the grain size of NZ first decreased and then increased.

(2) The maximum tensile strength of 542 MPa was achieved at the rotation speed of 900 rpm, equivalent to 85% of the base metal. The lower rotation speed could not generate sufficient heat input to make the complete joint, which led to poor properties, while high rotation speed caused overheating that turned the recrystallized grains coarse and poor properties.

(3) The main strengthening phases were $MgZn_2$, Al_2Cu, and AlCuMg. More phases precipitated in HAZ with the increase in the rotation speed for Al_2Cu, Al_2CuMg, and even the complex $Mg_{32}(Al,Zn)_{49}$. However, no complex phases precipitated in the NZ. Similar to HAZ, more phases precipitated in the NZ with an increase in the rotation speed.

(4) Large quantities of Al−Cu phases were precipitated in HAZ at the rotation speed of 900 rpm, while those precipitated in NZ at the rotation speed of 1500 rpm. The precipitated phases were caused by overheating in the joint, which led to tensile failure.

(5) With the increase in the rotating speed of the stirring head, the HAZ of the joint gradually became larger, and the low-hardness area of the HAZ increased and then decreased. The fracture was located in the softening zone or the area where the hardness was uneven.
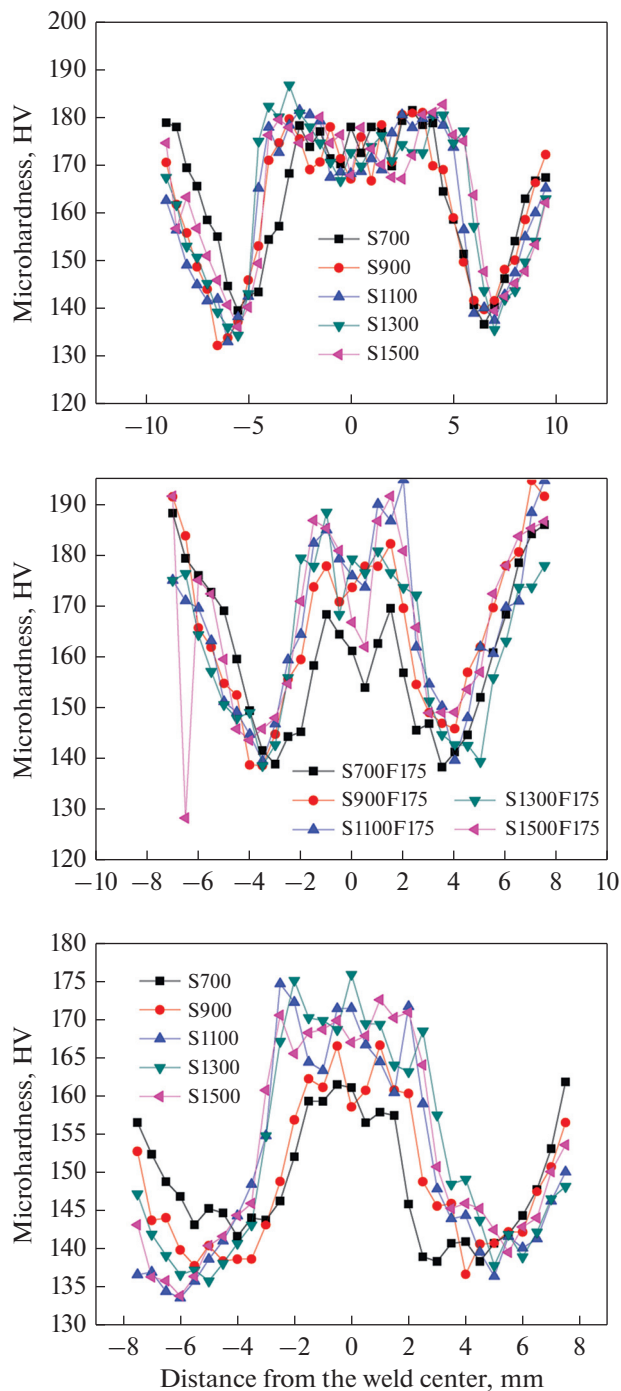
FUNDING

Fig. 8. Hardness profile of joints under different rotation speed. (a) The upper part; (b) the middle part; (c) the bottom part.

REFERENCES

1. M. M. Sharma, M. F. Amateau, and T. J. Eden, "Mesoscopic structure control of spray formed high strength Al−Zn−Mg−Cu alloys," Acta Mater. **53** (10), 2919−2924 (2015).

2. M. A. Milyaev, N. S. Bannikova, L. I. Naumova, V. V. Proglyado, E. I. Patrakov, I. Yu. Kamenskii, and V. V. Ustinov, "Magnetoresistance of CoFeNi/Cu superlattices differing in the ferromagnetic alloy composition," Phys. Met. Metallogr. **120** (9), 831−837 (2019).

3. F. Fadaeifard, M. R. Pakmanesh, M. Sh. Esfahani, K. A. Matori, and D. Chicot, "Nanoindentation analysis of friction stir welded 6061-T6 Al alloy in as-weld and post weld heat treatment," Phys Met. Metallogr. **120** (5), 483−491 (2019).

4. A. Shailesh Rao and N. Yuvaraja, "Comparison of appearance, microstructure and tensile properties during friction stir welding processes of Al−Si alloys," Phys. Met. Metallogr. **118** (7), 716−722 (2017).

5. M. M. Sharma, M. F. Amateau, and T. J. Eden, "Fatigue behavior of SiC particulate reinforced spray-formed 7XXX series Al-alloys," Mater. Des. **32** (8−9), 4304−4309 (2011).

6. Y. Jiang, Y. Zhao, Z. Zhao, K. Yan, L. Ren, and C. Du, "The strengthening mechanism of FSWed spray formed 7055 aluminum alloy under water mist cooling condition," Mater. Charact. **162**, 110185 (2020).

7. S. Ma, Y. Zhao, J. Pu, et al., "Effect of welding speed on performance of friction stir welded spray forming 7055 aluminum alloy," J. Manuf. Process. **46**, 304−316 (2019).

8. A. H. Feng, D. L. Chen, Z. Y. Ma, W. Y. Ma, and R. J. Song "Microstructure and strain hardening of a friction stir welded high-strength Al−Zn−Mg alloy," Acta Metall. Sin. **27** (4), 723−729 (2014).

9. W. Xu, Z. Li, and X. Sun, "Effect of welding speed on mechanical properties and the strain-hardening behavior of friction stir welded 7075 aluminum alloy joints," J. Mater. Eng. Perform. **26** (4), 1938−1946 (2017).

10. C. Zhang, G. Huang, Y. Cao, Y. Zhu, and Q. Liu, "On the microstructure and mechanical properties of similar and dissimilar AA7075 and AA2024 friction stir welding joints: Effect of rotational speed," J. Manuf. Process. **37**, 470−487 (2019).

11. Q. Wang, Z. Zhao, Y. Zhao, K. Yan, et al., "The adjustment strategy of welding parameters for spray formed 7055 aluminum alloy underwater friction stir welding joint," Mater. Des. **88**, 1366−1376 (2015).

12. F. Zhang, X. Su, Z. Chen, and Z. Nie, "Effect of welding parameters on microstructure and mechanical properties of friction stir welded joints of a super high strength Al−Zn−Mg−Cu aluminum alloy," Mater. Des. **67**, 483−491 (2015).

13. Q. Wang, Y. Zhao, K. Yan, et al., "Corrosion behavior of spray formed 7055 aluminum alloy joint welded by underwater friction stir welding," Mater. Des. **685**, 97−103 (2015).

14. Y. Zhao, Q. Wang, K. Yan, et al., "Microstructure and mechanical properties of spray formed 7055 aluminum alloy by underwater friction stir welding," Mater. Des. **56**, 725−730 (2014).